RSC Advances

ROYAL SOCIETY
OF CHEMISTRY

PAPER

View Article Online
View Journal | View Issue

Check for updates

Cite this: *RSC Adv.*, 2026, **16**, 19010

Bimetallic AuPt nanoparticles-based SERS substrate for high-performance endosulfan detection

Nguyen Dac Dien,[a] Xuan Hoa Vu,[b] Thi Thu Ha Pham,*[c] Pham Thi Nga,[bd] Tran Thu Trang,[b] Ngo Thi Lan,[b] Nguyen Van Hao,[b] Nguyen Thi Dung,[b] Thi Thu Thuy Nguyen,[c] Tran Thi Kim Chi,[e] Tran Thi Huong Giang,[f] Vuong Truong Xuan,[c] Trinh Danh Hung,[b] Lai Tong Anh Kiet,[c] Hoang Duy Long,[c] Do Duc Nguyen,[c] Pham The Tan,[g] Nguyen Vu Anh Tuyet[bh] and Truong Duc Cuong[i]

Surface-enhanced Raman spectroscopy (SERS) substrates based on metallic or alloy nanomaterials have attracted increasing attention for trace pesticide detection in food and environmental samples. Endosulfan (ES), a chemically stable and hazardous organochlorine pesticide, remains difficult to be rapidly and sensitively detected at low concentration. In this work, a SERS substrate based on bimetallic AuPt nanoparticles (NPs) was developed *via* reduction of $HAuCl_4$ and H_2PtCl_6 precursors. The resulting AuPt nanomaterials were systematically characterized using TEM, HRTEM, XRD, EDS, and UV-vis, and their SERS performance was evaluated using endosulfan as a probe analyte. Among the investigated compositions, AuPt NPs with an Au : Pt molar ratio of 1 : 1 exhibited the best analytical performance, with an enhancement factor (EF) of approximately 14.3×10^6, a limit of detection (LOD) of 0.05 ppm (1.225×10^{-7} M), and a good linear relationship between log *I* and log *C* over the concentration range of 0.05–2 ppm. The developed substrate also showed good repeatability, signal uniformity, and storage stability. The enhanced SERS performance is likely associated with the combined effects of alloy composition and favorable nanoparticle morphology, particularly the formation of interparticle nanogaps that promote hotspot generation. Based on the present results, the electromagnetic contribution is considered to be the dominant enhancement mechanism, while electronic interactions between AuPt NPs and ES molecules may provide a supportive contribution. These results suggest that AuPt NPs are a promising SERS-active platform for sensitive endosulfan detection.

Received 28th February 2026
Accepted 6th April 2026

DOI: 10.1039/d6ra01752e

rsc.li/rsc-advances

1. Introduction

Endosulfan (ES) is an organochlorine pesticide (OCP) that has been widely used in agriculture because of its high insecticidal efficiency against a broad range of pests affecting crops, fruits, vegetables, cereals, cotton, and ornamental plants. Despite its effectiveness, ES has become a major environmental and public health concern because of its high persistence, low water solubility, hydrophobic nature, and strong tendency to accumulate in soil, sediment, and the food chain.[1–3] Its residues and degradation products, particularly endosulfan sulfate, may remain in environmental and food-related matrices for extended periods, thereby increasing the risk of chronic exposure. ES has been associated with adverse effects on aquatic organisms and has also been linked to neurotoxic, reproductive, teratogenic, mutagenic, and other long-term health effects in humans.[2,3] Therefore, the development of reliable analytical methods for monitoring ES residues in water, food, and environmental samples remains an important task. Endosulfan ($C_9H_6C_{16}O_3S$) exists as two stereoisomeric forms, namely α-endosulfan and β-endosulfan (Fig. 1).[4]

A variety of analytical techniques have been employed for the determination of organochlorine pesticides and ES, including chromatographic and mass spectrometric methods.[5] These techniques generally provide high sensitivity and reliable

---

[a] Faculty of Occupational Safety and Health, Vietnam Trade Union University, 169 Tay Son Street, Kim Lien Ward, Ha Noi City 10000, Vietnam

[b] Institute of Science and Technology, TNU-University of Sciences, Phan Dinh Phung Ward, Thai Nguyen province 24000, Vietnam

[c] Faculty of Chemistry, TNU-University of Sciences, Phan Dinh Phung Ward, Thai Nguyen province 24000, Vietnam. E-mail: haptt@tnus.edu.vn

[d] Faculty of Secondary School, Hoa Lu University, 2 Xuan Thanh Street, Hoa Lu Ward, Ninh Binh province, Vietnam

[e] School of Electrical and Electronic Engineering, Hanoi University of Industry, 298 Cau Dien, Tay Tuu, Hanoi, Vietnam

[f] Institute of Materials Science, Vietnam Academy of Science and Technology, 18 Hoang Quoc Viet Road, Nghia Do Ward, Ha Noi City 10000, Vietnam

[g] Hung Yen University of Technology and Education, Viet Tien Ward, Hung Yen Province, Vietnam

[h] Hung Yen High School for the Gifted, 1 Chu Van An, Pho Hien, Hung Yen, Vietnam

[i] Quang Ninh Provincial Center for Vocational Training-Continuing Education, Group 45, Cao Thang 5 Area, Ha Lam Ward, Quang Ninh Province, Vietnam

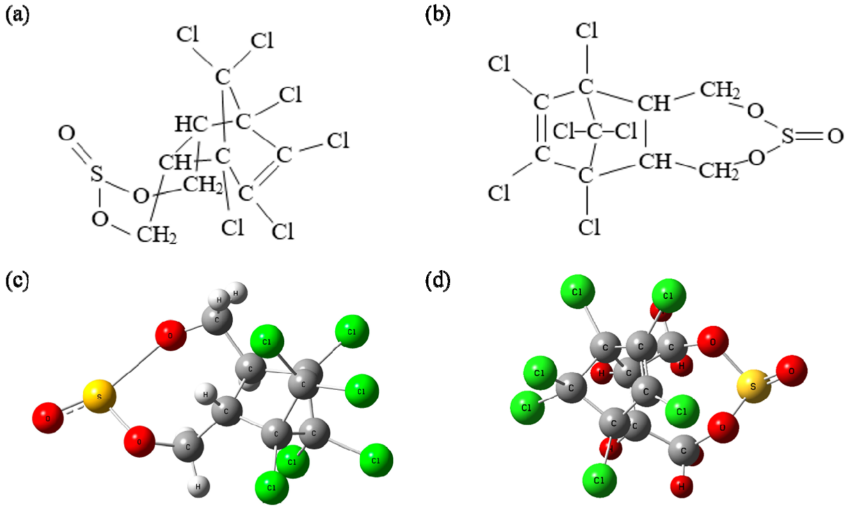

Fig. 1 Molecular structures of endosulfan isomers: (a and c) α-endosulfan and (b and d) β-endosulfan.[4]

identification in complex matrices; however, they usually require expensive instrumentation, laborious sample pretreatment, and trained personnel. Such limitations have stimulated interest in simpler and faster analytical strategies for trace pesticide detection. Among them, surface-enhanced Raman scattering (SERS) has emerged as a promising alternative because it combines rapid analysis, high sensitivity, molecular fingerprint information, and nondestructive detection.[6] Owing to these advantages, SERS has attracted increasing attention in food safety and environmental analysis.

The analytical performance of SERS strongly depends on the properties of the substrate. Signal enhancement mainly arises from localized electromagnetic field amplification near plasmonic nanostructures and is therefore highly sensitive to the composition, size, morphology, and spatial arrangement of the sensing material.[7–11] Noble-metal nanostructures, especially Au- and Ag-based materials, have been extensively explored as SERS-active substrates because of their favorable plasmonic characteristics and tunable surface chemistry.[12–15] Recent studies have shown that the design of nanostructured substrates plays a central role in improving sensitivity, reproducibility, and practical applicability in SERS-based analysis.[16–19]

In this context, bimetallic nanomaterials have attracted considerable interest because they can integrate the advantageous features of two metals within a single nanostructure. Compared with monometallic systems, bimetallic substrates may exhibit improved structural tunability, surface activity, chemical stability, and analytical performance.[20–26] In particular, Au-based bimetallic systems are attractive for SERS applications because Au provides strong plasmonic activity and good chemical stability, while the second metal can modify the electronic structure and surface-related properties of the substrate. Although Pt itself is generally not regarded as an efficient standalone SERS material in the visible region, it remains highly attractive because of its chemical stability and distinctive physicochemical properties.[27–31] Therefore, combining Pt with Au may provide a useful approach for tuning both the interfacial properties and the sensing behavior of SERS-active nanostructures.

Representative studies have demonstrated that bimetallic nanostructures can outperform their monometallic counterparts in SERS applications.[32–35] Moreover, porous or discontinuous nanostructures may provide more accessible active sites and facilitate analyte localization near plasmonic hotspots, thereby improving signal enhancement.[36,37] Bimetallic nanoparticles have thus become increasingly attractive for SERS-based detection of environmentally relevant and food-related analytes.[24–26] Nevertheless, reports specifically focusing on SERS-active substrates for endosulfan detection remain limited.[38] Since the physicochemical properties of bimetallic nanocrystals can be tuned through composition, size, morphology, and structure,[39] AuPt nanoparticles are of particular interest as candidate substrates for ES detection.

In this work, bimetallic AuPt nanoparticles with different Au : Pt molar ratios were synthesized *via* a reduction route using $HAuCl_4$ and H_2PtCl_6 as precursors. The resulting nanomaterials were evaluated as SERS-active substrates for endosulfan detection, with particular attention to the effect of composition on sensitivity and reproducibility. By focusing on AuPt alloy nanoparticles, this study aims to provide a simple and effective SERS platform for sensitive ES detection and to further explore the potential of composition-tunable bimetallic nanostructures for pesticide-oriented SERS analysis.

2. Experimental

2.1. Chemicals and reagents

Chloroauric acid trihydrate ($HAuCl_4 \cdot 3H_2O$, 99.9%), chloroplatinic acid hexahydrate ($H_2PtCl_6 \cdot 6H_2O$, 99%), trisodium citrate dihydrate (TSC, $Na_3C_6H_5O_7 \cdot 2H_2O$, 99.5%), L-ascorbic acid (L-AA, $C_6H_8O_6$, 99.7%), sodium borohydride ($NaBH_4$, 98%), polyvinylpyrrolidone (PVP, $(C_6H_9NO)_n$), and absolute ethanol (C_2H_5OH) were procured from Merck. All chemicals were of analytical grade and used as received without additional

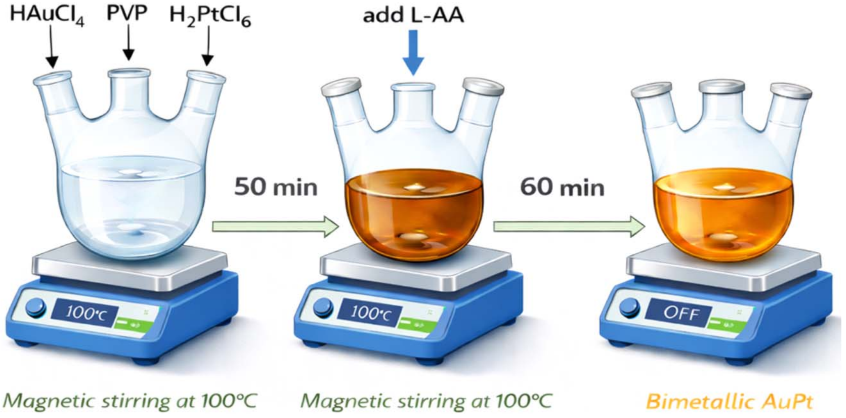

Fig. 2 Synthesis process for bimetallic AuPt nanoparticles.

purification. The pesticide used for the SERS measurement was endosulfan ($C_9H_6Cl_6O_3S$, 99%) (analytical standard, Sigma-Aldrich). The solvent for changing the ES solution concentration was ethanol. The polished glass plates were provided by Zhejiang Lijing Optoelectronics Technology Co., Ltd Double distilled water supplied by a Milli-Q purification system, was used in preparing the aqueous solutions. All glassware was cleaned thoroughly prior to use with distilled water.

2.2. Synthesis of Au NPs

As we know, the most common method for producing monometallic nanocrystals is the reduction of metal salt in a proper reductant. In this study, Au NPs were prepared by a chemical reduction technique, in which $HAuCl_4$ was chosen as metal salt and TSC as reducing agent. In a typical procedure, 0.1 g $HAuCl_4 \cdot 3H_2O$ salt was dispersed in 10 ml distilled water using magnetic stirrer equipped with a Teflon coated magnetic stir bar to achieve $HAuCl_4$ solution (concentration of 25 mM), then heated to 100 °C. Any stock of $HAuCl_4$ was kept protected from light. Then, 0.5 ml of 50 mM TSC solution was added and mixed evenly with continuous stirring for 20 min to reduce Au^{3+} ions to Au^0 atoms as following:

$$6HAuCl_4 + Na_3C_6H_5O_7 + 5H_2O \rightarrow 6Au + 6CO_2\uparrow + 3NaCl + 21HCl \quad (1)$$

A purple-coloured Au seed solution was obtained and Au atoms aggregated into spherical gold nanoparticles (Au NPs). The final mixture was naturally cooled to room temperature, then washed with distilled water and absolute ethanol several times *via* redispersion/filtration cycles to remove remains and by-products to obtain Au NPs precipitate.

2.3. Synthesis of Pt NPs

Briefly, 0.15 ml of 20 mM H_2PtCl_6 solution was mixed with 12 ml distilled water and 0.2 ml of 3.7 mM PVP under continuously stirring for 20 min at room temperature. Then, 0.15 ml of 20 mM $NaBH_4$ solution was dropwise added to the above mixture and stirred for 30 min, Pt^{4+} was reduced to Pt^0 as follows:

$$NaBH_4 + H_2PtCl_6 + 3H_2O \rightarrow Pt^0 + NaCl + 5HCl + B(OH)_3 + 2H_2\uparrow \quad (2)$$

The obtained mixture was filtered with distilled water several times to achieve Pt NPs.

2.4. Synthesis of bimetallic AuPt nanoparticles

The similar strategy was also applied to synthesize bimetallic nanocrystals, in which we reduced two kinds of metal salts together. However, it is difficult to simultaneously control the reduction and nucleation process of two types of metals because their redox potentials are different. $NaBH_4$ is a strong reducer, both Au^{3+} and Pt^{4+} can be reduced instantly and the process is difficult to control. In order to avoid separate nucleation of two metals, we select L-AA as proper reducing agent to separate effectively nucleation and growth into two distinct steps and aqueous solutions of $HAuCl_4$ and H_2PtCl_6 as the reaction system to produce alloy. L-AA is weak reducing agent that better controls the nucleation and growth process. Additionally, the absence of proper surfactant makes it difficult to prevent the particles from aggregating. In this research, PVP was used as surfactant.

In a typical synthesis, the growth solution was prepared in a 250 ml reaction flask containing H_2O (100 ml), $HAuCl_4$ (0.48 ml, 25 mM), PVP (0.3 ml, 3.4 mM), freshly prepared H_2PtCl_6 (25 mM) solution and stirred using a magnetic stirring bar. The mixture was heated to 100 °C and kept for 50 min. Then, 1.4 ml L-AA (50 mM) was gradually added under continuous stirring for 60 min at 100 °C, the solution colour changed gradually from white to brown (Fig. 2). L-AA played the role of reducing agent in creating Au and Pt atoms as following equations:

$$3C_6H_8O_6 + 20HAuCl_4 + 18H_2O \rightarrow 20Au\downarrow + 18CO_2\uparrow + 80HCl \quad (3)$$

$$C_6H_8O_6 + 5H_2PtCl_6 + 6H_2O \rightarrow Pt\downarrow + 6CO_2\uparrow + 30HCl \quad (4)$$

After stirring, the stir bar was removed, the mixture was covered with parafilm and allowed to cool down to room temperature for an additional 3 h. Next, bimetallic AuPt NPs were collected through filtering and redispersing in distilled water or absolute ethanol several times to remove residual impurities, followed by air-drying at room temperature. Au : Pt molar ratio of the product was changed by precisely adjusting the volume of H_2PtCl_6 as 0.16, 0.32, 0.48, 0.64, and 0.8 ml. The corresponding series of AuPt NPs were denoted as Au_3Pt_1, Au_3Pt_2, Au_3Pt_3, Au_3Pt_4, Au_3Pt_5 according to Au : Pt molar ratios of 3 : 1, 3 : 2, 1 : 1, 3 : 4, and 3 : 5, respectively.

2.5. Fabrication of SERS substrate

Square glass plate (0.5 cm × 0.5 cm) was washed with water and ethanol and finally blow-dried with air. SERS substrates were prepared on glass surfaces using a self-assembly technique. The Au, Pt, AuPt NPs colloids were coated onto the surface of a glass plate. The substrates were further dried at 60 °C for 1 h in an oven to form a dense film which plays a role of sensing layer composed of monometallic or bimetallic NPs. Endosulfan was used as a Raman probe to evaluate the SERS property of this Au, Pt, or AuPt materials. ES solutions with five desired concentrations, namely 0.05, 0.15, 0.5, 1.2, and 2 ppm were obtained by dissolving the appropriate amount of ES in 0.5 ml of ethanol in an ultrasonic bath. 2 μl of ES at the required concentration was dropped on glass wafer or Au, Pt, AuPt NPs substrates and shaken for 1 min to ensure homogeneity, then let dry at room temperature.

2.6. Instrumentation

Transmission electron microscopy (TEM) images were captured on a JEOL-2010 (Japan) operating at an accelerated voltage of 200 kV to characterize the morphology of nanoparticles. The lattice constants were identified using high-resolution TEM (HRTEM, JEOL JEM-F200, Japan). X-ray diffraction (XRD) patterns were recorded using Bruker D8 Advance diffractometer (Germany) with Cu-K_α radiation ($\lambda = 1.5418$ Å) to determine the crystal phase structure of the as-synthesized samples over the Bragg angle region between 30° to 80° with a scanning rate of 6° min^{-1}. Energy-dispersive X-ray spectroscopy (EDS) measurement was conducted using Hitachi SU 8020 (Japan). Ultraviolet-visible (UV-vis) absorption spectra were obtained by JASCO V770 spectrometer (Japan) to investigate the optical property. Raman spectra were collected in a darkroom using an EnSpectr R532 confocal microscope equipped with a 532 nm diode excitation laser with 3 mW of laser power. The excitation beam was focused onto the sample with a focal spot size of approximately 2 μm and 5-second integration time. Samples were measured 3 times in a random order and averaged from the collected spectra. The reference Raman spectrum of ES powder on glass slides was recorded. SERS sensor properties such as sensitivity and reproducibility towards ES detection were observed in this research.

2.7. Calculation method of density functional theory (DFT)

Density function theory (DFT) geometric optimization calculations were performed using the Vienna *Ab initio* Simulation Package (VASP). DFT harmonic vibrational frequency calculations were performed using the Gaussian 09 program at the B3LYP level with a hybrid basis set of 6–31 G(d,p) and lanL2DZ. ES can be easily identified by the peaks of the SERS spectra calculated by DFT.

3. Results and discussion

3.1. Characterization of Au NPs and Pt NPs

We carried out an XRD analysis to obtain the nanoparticles' structure. The results are shown in Fig. 3, the XRD patterns with sharp diffraction peaks indicate that the Au and Pt NPs were well crystalline. There are four diffraction peaks at 2θ values of 38.2°, 44.4°, 64.6°, and 77.6° corresponding to (111), (200), (220), and (311) crystalline planes for Au FCC (face-centered cubic, JCPDS 04-0784)[40] (Fig. 3a). Fig. 3b demonstrates 3 diffraction peaks at 2θ of 39.6°, 46.2°, and 67.6° that indexed into (111), (200), and (220) crystalline planes for Pt FCC (JCPDS 04-0802).[31] Based on the intensity of the XRD diffractogram, the favored growth direction of crystals is the (111) plane with a lattice constant of 3.99 Å.[41]

TEM images were used to identify the surface morphology features and particle size distribution of Au and Pt NPs. The TEM image of Au NPs in Fig. 4a shows the monodispersal

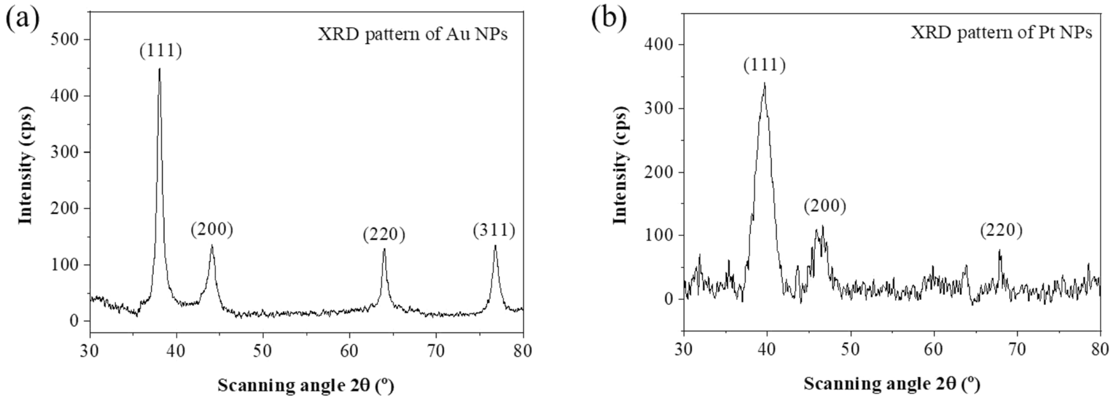

Fig. 3 XRD pattern of (a) Au NPs, (b) Pt NPs.

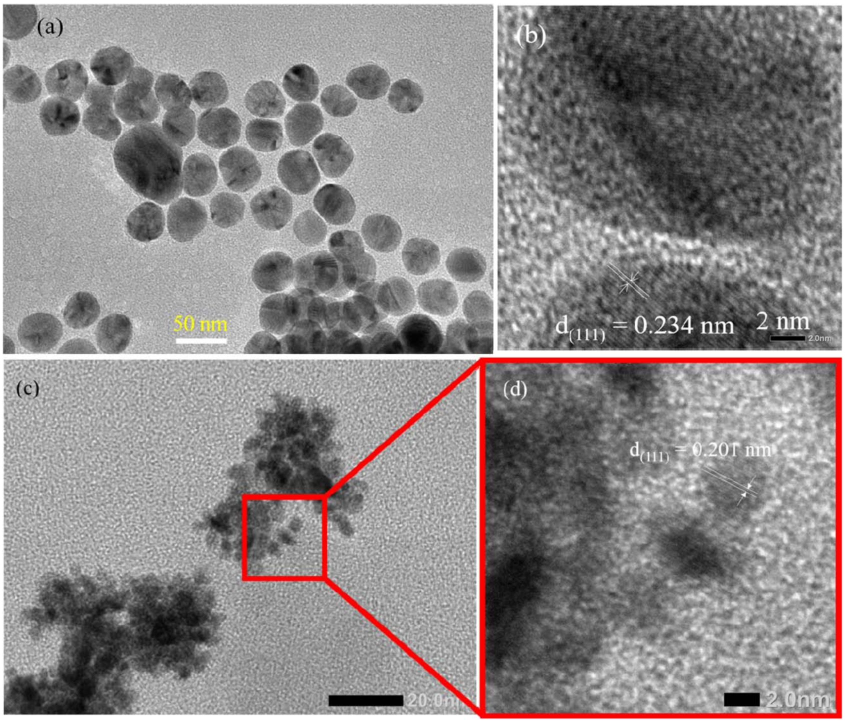

Fig. 4 (a) TEM, (b) HRTEM images of Au NPs; (c) TEM, (d) HRTEM images of Pt NPs.

pseudo-spherical morphology with the average diameter of 40 nm. It is also found that Au NPs are uniform with low-density growth. The synthesized Pt NPs exhibited agglomeration of particles with an asymmetrical configuration and average diameter of ~5 nm. HRTEM results of obtained Au NPs and Pt NPs can be observed that the 0.234 nm and 0.201 nm lattice spacing correspond to the (111) crystal planes of Au and Pt (Fig. 4b and d).

3.2. Characterization of bimetallic AuPt nanoparticles

The co-reduction strategy can control the structure of bimetallic nanocrystals using the different redox potential between Au and Pt. The standard redox potential of $PtCl_6^{2-}$/Pt pair was higher than that of $AuCl_4^-$/Au pair, so Au^{3+} ions were reduced more preferably than Pt^{4+} ions. After the reduction of Au^{3+}, its chemical behavior determines the final structure of products. Au atoms diffuse into the crystal lattice of Pt, leading to the formation of Au–Pt bonds, intermetallic or alloyed compounds were synthesized. The surfactant, *i.e.* PVP, slows the generation of metal atoms, so clusters formed in the nucleation stage are easier to coalesce. PVP promotes anisotropic crystal growth in AuPt due to the disruption of symmetrical crystal growth and surface passivation processes. Using the same $HAuCl_4$ amount, we synthesized five AuPt NPs with varying Au : Pt molar ratios by simply adjusting the volume of H_2PtCl_6 solution.

The color of the mixture solution changed from milky-white to dark purple due to the formation of bimetallic AuPt NPs. TEM image shown in Fig. 5a reveals particle-like morphology and confirms the monodispersity of these bimetallic AuPt nanocrystals which facilitates the diffusion of target molecules, therefore enhances SERS performance. The discontinuous distribution of 10–20 nm AuPt NPs create many nanogaps which generate intense localized plasmon hotspots under light excitation.[42] The superior SERS performance of the Au_3Pt_3 sample is likely associated not only with its Au–Pt compositional balance but also with its favorable morphological characteristics. In particular, the discontinuous particle distribution and the resulting interparticle nanogaps can promote hotspot generation, thereby enhancing the local electromagnetic field. Thus, the present results suggest a composition-dependent morphology-activity correlation, although a more systematic investigation of particle size, shape, and gap-distance effects will be needed for a full structure-performance understanding. The shape of the AuPt NPs becomes rounded with the increase of H_2PtCl_6 amount beyond 0.64 ml (Au_3Pt_4, Au_3Pt_5), inferring fewer high-energy sites in the AuPt NPs. The diameter and density of the product also increase with the Au : Pt molar ratio.

The high-resolution TEM (HRTEM) image of the Au_3Pt_3 sample in Fig. 5f reveals two distinct lattice fringes. The lattice spacing of 0.234 nm corresponds to the (111) dominant crystal plane of Au, while the 0.201 nm spacing is assigned to the (111) plane of Pt. The lattice spacing of 0.221 nm is attributed to the (111) plane of the AuPt alloy, meaning that Au, Pt, and AuPt NPs are distinctly found.

EDS measurement of AuPt NPs is displayed in Fig. 6a, only Au and Pt elements are detected. EDS analysis reveals that Au_3Pt_3 NPs consist of 80.8 wt% Au and 19.2 wt% Pt. The composition of bimetallic nanocrystals can be controlled by changing the molar ratio of two metal precursors. However, a smaller proportion of Pt was reduced and alloyed with Au

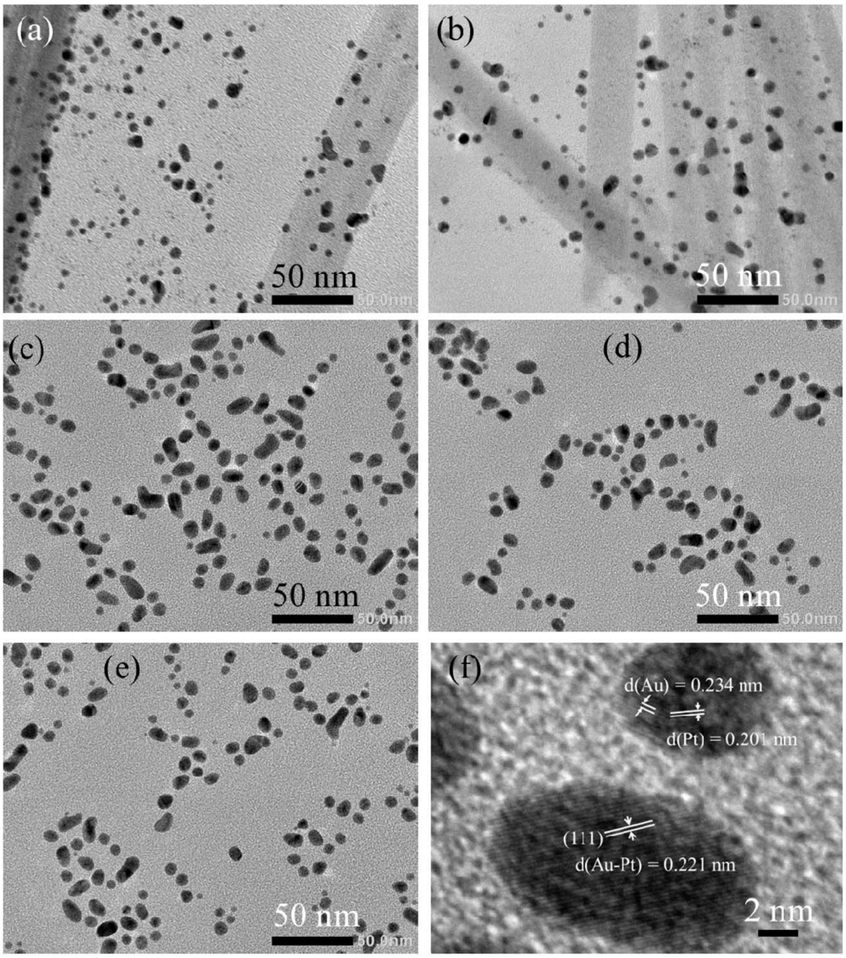

Fig. 5 TEM images of sample: (a) Au_3Pt_1, (b) Au_3Pt_2, (c) Au_3Pt_3, (d) Au_3Pt_4, (e) Au_3Pt_5 and (f) HRTEM of Au_3Pt_3 NPs.

because the redox potential of Pt is higher than that of Au, so the composition in final products is not consistent with the feeding ratio. Aside from the primary elements of Au and Pt, Cu and C signals observed in the EDS spectrum come from the carbon-coated Cu grid used for EDS sample analyzing. A small amount of O elements was present on the surface of AuPt nanocrystals due to inevitable surface oxidation during sample preparation.[43]

The XRD patterns in Fig. 6b indicate that distinct diffraction peaks corresponding to Au are observed alongside the Pt diffraction peaks. Comparing the XRD patterns of pure Au (Fig. 3a), pure Pt (Fig. 3b), diffraction peaks corresponding to individual Au and Pt atomic positions are observed without any shifting of the peaks. Sharp diffraction peaks corresponding to Au appear, lower and broader peaks compared to those of Au are likely related to the presence of Pt, indicating that the size of Pt crystals is significantly smaller than that of the Au crystals. As the Pt amount increased, the diffraction intensity of the Pt (111) facet progressively increased, while the Au (111) peak intensity decreased. The high-energy plane, *i.e.* Au (200) reaches maximum at Au_3Pt_3 that promises high SERS activity. Interestingly, the characteristic peaks of individual metals fade and new Bragg reflections can be observed at approximately 32°, 56.5°, and 75°, which cannot be indexed to either Au or Pt alone. These diffraction peaks indicating the presence of an additional phase in the structure are indexed to the AuPt alloy, consistent with previous report.[44,45] These results confirm that bimetallic AuPt NPs have been successfully prepared. The crystalline size of Au NPs was calculated using the Debye–Scherrer formula:[46]

$$D = \frac{k\lambda}{\beta \cos \theta}$$

where $k = 0.893$ is the Scherrer constant, $\lambda = 0.15418$ nm is the wavelength of X-ray irradiation (Cu-K_α), β is the full width at half maximum of (111) peak, θ is Bragg diffraction angle, and D is the crystalline size. The average crystalline size of Au, Pt, Au_3Pt_1, Au_3Pt_3, and Au_3Pt_5 NPs were approximately 12 nm, 3.66 nm, 5.9 nm, 6.5 nm, and 5.1 nm, respectively (Fig. 6c).

The isolated spherical gold nanoparticles in dispersion provide plasmon resonances in the spectral range of 515–550 nm. The bigger the nanoparticles, the more red-shift the plasmon resonance.[47] The UV-vis spectra of Au, Pt, AuPt samples with different Au : Pt molar ratios were exhibited in Fig. 7a. Au NPs are characterized by a marked optical absorption at a wavelength of 521 nm. The position of the absorption peaks unchanged at 521 nm, indicating the structure remains intact.

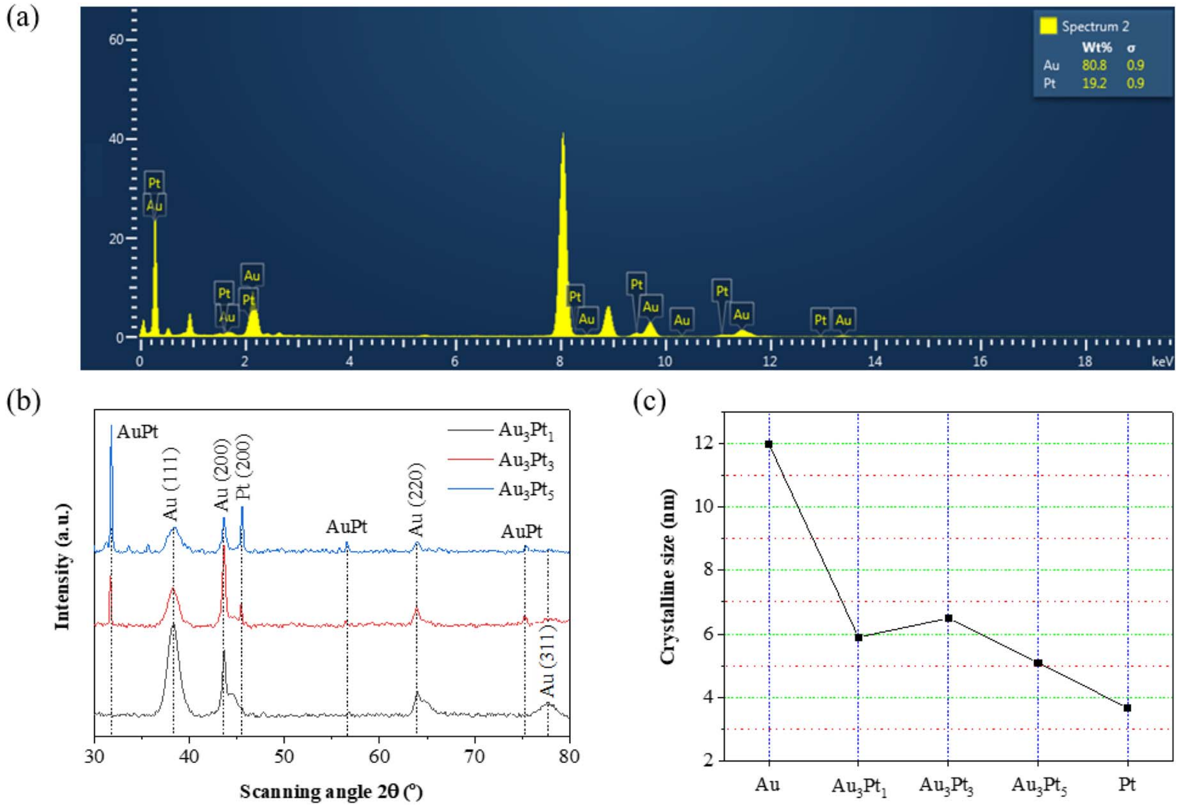

Fig. 6 (a) EDS spectrum of Au_3Pt_3 NPs, (b) XRD patterns of Au_3Pt_1, Au_3Pt_3, and Au_3Pt_5 NPs, (c) crystalline size of pristine Au, Pt NPs, and AuPt NPs.

In addition, the plasmon extinction peak of AuPt broadened and weakened with increasing Pt component (Fig. 7b). For AuPt NPs, the plasmon absorption range spans from the visible to near-infrared region and the 532 nm laser, which is closer to the plasmon resonance of AuPt NPs, is chosen to conduct SERS measurements because of the small size of AuPt NPs (10–20 nm). For larger size Au NPs (80 nm), 633 and 785 nm lasers are typically used.[48] The only change observed in the absorbance spectra was a decrease in the maximum peak intensity at 521 nm when the Au : Pt molar ratio decreased from 3 : 1 to 3 : 5. Gap-plasmon resonances at the interparticle junction are highly sensitive to the interparticle distance.

3.3. Calculated Raman spectra of ES on AuPt model

The calculated Raman spectrum of ES on the AuPt model is shown in Fig. 8a. In the calculated spectra, the SERS peaks of ES are dominated by the C–C=C in-plane stretching vibration (~1645 cm^{-1}), with other weaker peaks, different from the experimental spectra. The experimental spectrum (Fig. 8b) shows two main Raman bands of H–C–H out-of-plane bending

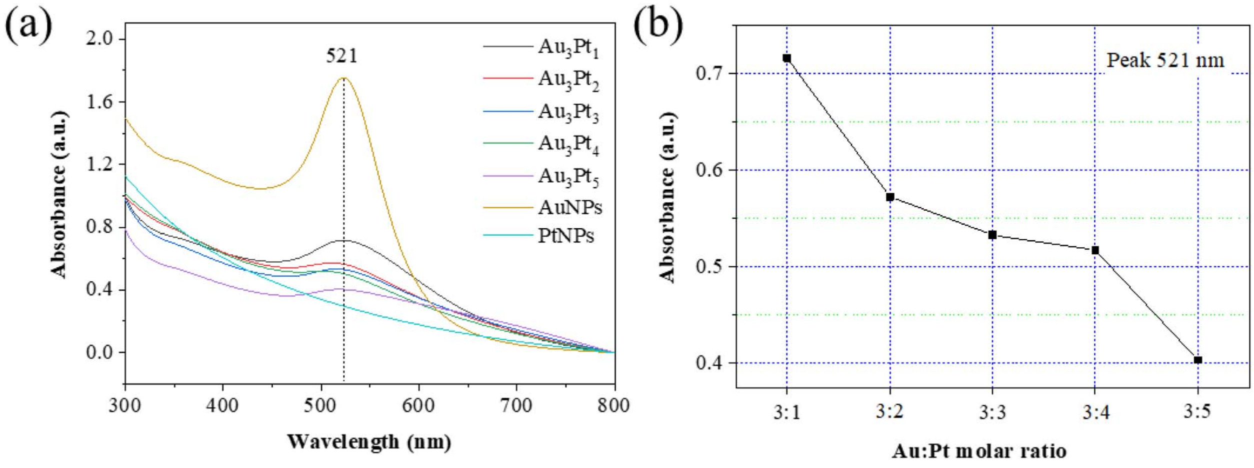

Fig. 7 (a) UV-vis absorption spectra of AuPt samples, (b) the dependence of peak absorbance on Au : Pt molar ratio.

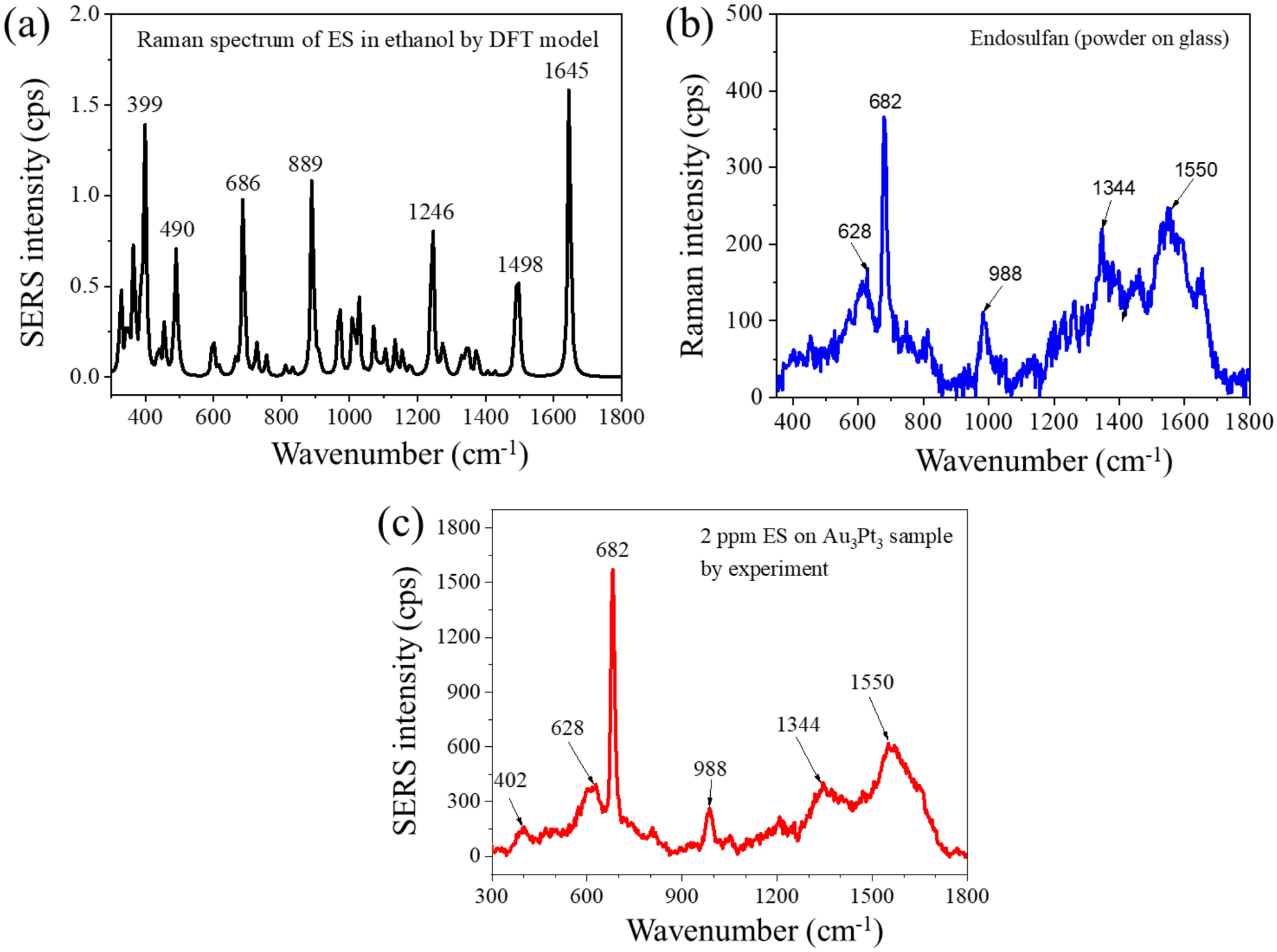

Fig. 8 (a) Calculated Raman spectrum of 2 ppm ES model using DFT frequency calculation, (b) Raman spectrum of powder ES on glass wafer, (c) experiment Raman spectrum of 2 ppm ES on real Au_3Pt_3 sample for comparison.

centered at 682 cm^{-1} and H–C–O out-of-plane bending at 1550 cm^{-1}. Fig. 8c shows the experiment Raman spectrum of 2 ppm ES on real Au_3Pt_3 sample for comparison. Table 1 summaries the characteristic vibrations of ES molecules from DFT and experiment. The band at ~490 cm^{-1} may be associated with the interaction of the S=O-containing group of ES with the AuPt surface, suggesting possible interfacial adsorption of the molecule on the substrate. However, the exact bonding configuration cannot be conclusively assigned from the present data alone. The peaks observed at 889, 1246, and 1498 cm^{-1}, which were not observed in the experiment, are assigned to Cl–C=C rocking, Cl–C–C bending, and C–C–O asymmetric stretching, respectively. The symmetric stretching vibration of the Cl–C–Cl bond shifts from 399 cm^{-1} to 402 cm^{-1}, the out-of-plane

Table 1 Characteristic vibrations of ES molecules from DFT and experiment

Calculations (cm^{-1})	Experiment (cm^{-1})	Characteristic vibration	Vibration modes
399	402	Cl–C–Cl	Symmetric stretching
490		O–S=O	Rocking
	628	O–S–O	Bending
686	682	H–C–H	Out-of-plane bending
889		Cl–C=C	Rocking
	988	C–C–C	Bending
1246		Cl–C–C	Bending
	1344	H–C–C	Bending
1498		C–C–O	Asymmetric stretching
	1550	H–C–O	Bending
1645		C–C=C	In-plane stretching vibration

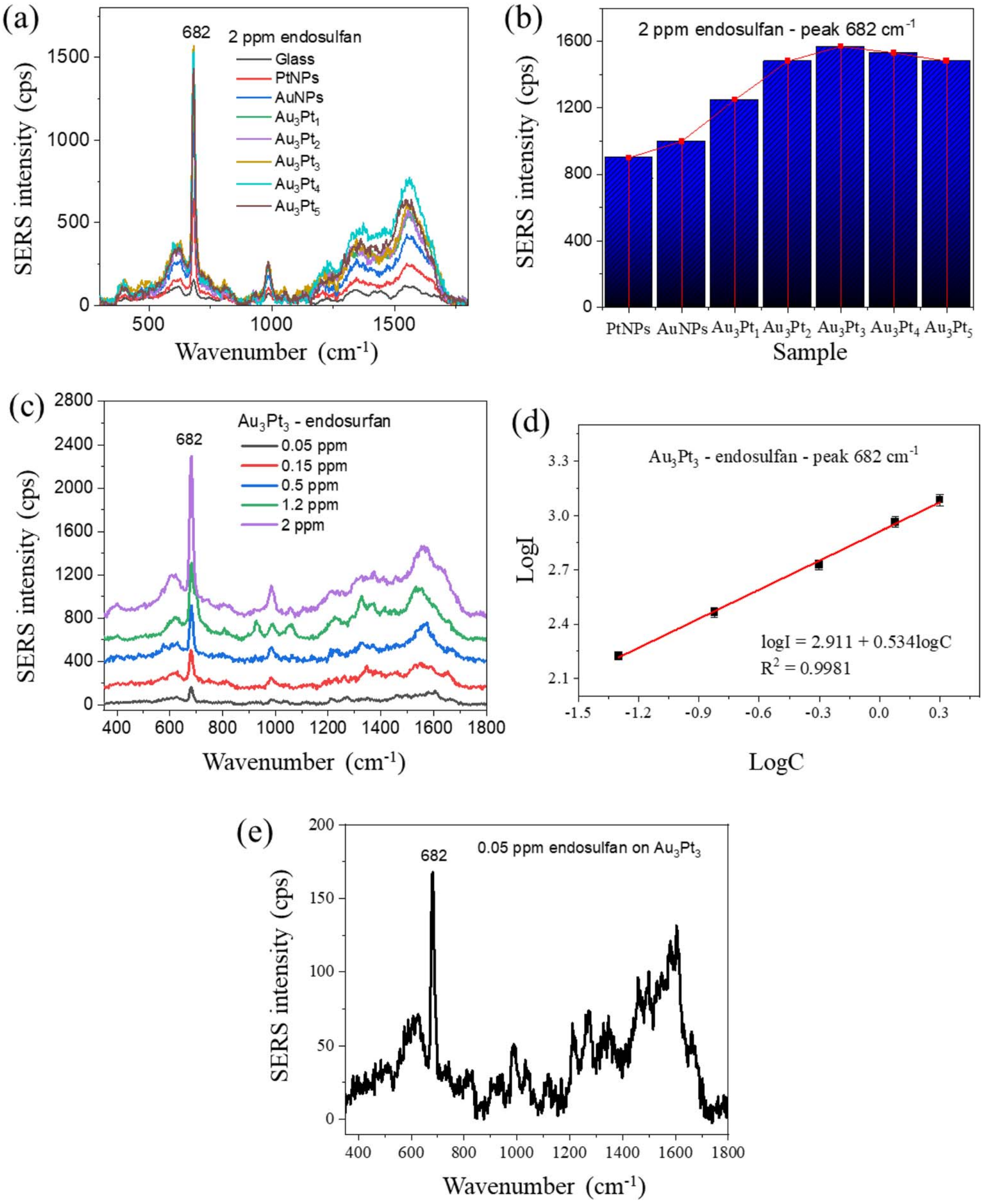

Fig. 9 (a) SERS spectra of 2 ppm endosulfan on glass, pristine Au NPs, Pt NPs, and AuPt substrates with different Au : Pt ratios, (b) the SERS intensity of 682 cm^{-1} peak as a function of samples, (c) SERS spectra of Au_3Pt_3 towards different concentrations of endosulfan in the range of 0.05–2 ppm, (d) linear relationship between SERS intensity of 682 cm^{-1} peak and endosulfan concentration in logarithm scale, (e) SERS spectrum of 0.05 ppm ES on Au_3Pt_3.

bending vibration of H–C–H bond shifts from 686 cm^{-1} to 682 cm^{-1}, consistent with experimental results.

3.4. SERS performance of bimetallic AuPt NPs towards endosulfan

Endosulfan (ES) was used as a SERS-sensitive probe molecule to evaluate the SERS enhancement over the as-synthesized AuPt NPs. A layer of Au NPs, Pt NPs, AuPt NPs anchored on a glass plate served as the SERS substrate for collecting the SERS spectra of ES molecules. The sensitivity of the SERS substrates was studied by observing the Raman spectra of ES on a glass surface and on the AuPt surface. To evaluate the effect of Au : Pt ratio on the SERS property of the nanostructures in the detection of ES, we used the same solution concentration of 2 ppm and the results were shown in Fig. 9a.

SERS spectra were collected from six different spots of each substrate to minimize measurement error. The characteristic peaks of ES on the AuPt surface match those observed for ES on the glass surface. The SERS signal intensity collected from endosulfan on glass substrate was insignificant. Clearly, the AuPt substrates with different Au : Pt ratios exhibit a much higher SERS intensity upon ES exposure compared to glass substrate. The presence of AuPt NPs leads to Raman signal enhancement from ES molecules. The molar ratio of Au and Pt plays a critical role in the SERS performance. The molar ratio of 1 : 1 is the most favourable for forming AuPt alloy NPs, which

Table 2 Comparison of AuPt NPs with other SERS substrates in detecting ES

Materials	EF	LOD	Ref.
Ag NPs	No report	8.9×10^{-7} M	16
CNT/PANI/SbO	No report	5.22×10^{-6} M	50
AuPt NPs	14.3×10^{6}	1.225×10^{-7} M	This work

exhibited the optimal SERS performance (Fig. 9b). Lower ratio results in smaller NPs, the smaller gaps between neighboring nanoparticles, the lower hotspot intensity, reducing the SERS performance. Higher ratio increases the size of NPs and decreases effective surface area for absorption of target molecules, so the plasmon effect of Au sharply decreases, but the weak plasmon effect of Pt gradually increases, resulting in the lower hotspot intensity, ultimately weakening the SERS activity.

The analytical enhancement factor (EF) is a quantitative value used to describe the signal enhancement and is defined by:[49]

$$\mathrm{EF} = \frac{I_{\mathrm{SERS}}}{I_{\mathrm{nor}}} \frac{C_{\mathrm{nor}}}{C_{\mathrm{SERS}}} \tag{5}$$

where I_{SERS} is Raman signal intensity when the SERS system is present, I_{nor} is Raman signal intensity of non-SERS when the SERS system is absent, C_{SERS} is the concentration of ES molecule used with the SERS system, C_{nor} is the concentration of the ES molecule used without the SERS system.

Among characteristic peaks at 682, 985, 1575 cm^{-1}, 682 cm^{-1} peak exhibited the best performance across all tested concentrations, thus was selected to calculate the enhancement factor of these SERS substrates. The EF for ES concentration of 0.05 ppm adsorbed on the Au_3Pt_3 NPs was calculated to be 14.3 $\times$ 10^{6}. The field enhancement of AuPt NPs samples first increased and then decreased as the Pt portion increased, experiencing a maximum value pointed to the Au_3Pt_3 NPs (Fig. 9b). This sample creates hotspots exhibiting strong field enhancement, provides lots of active sites for ES molecules adsorption, and significantly enhances the Raman scattering of adsorbed molecules. Au_3Pt_3 NPs possess the strongest local

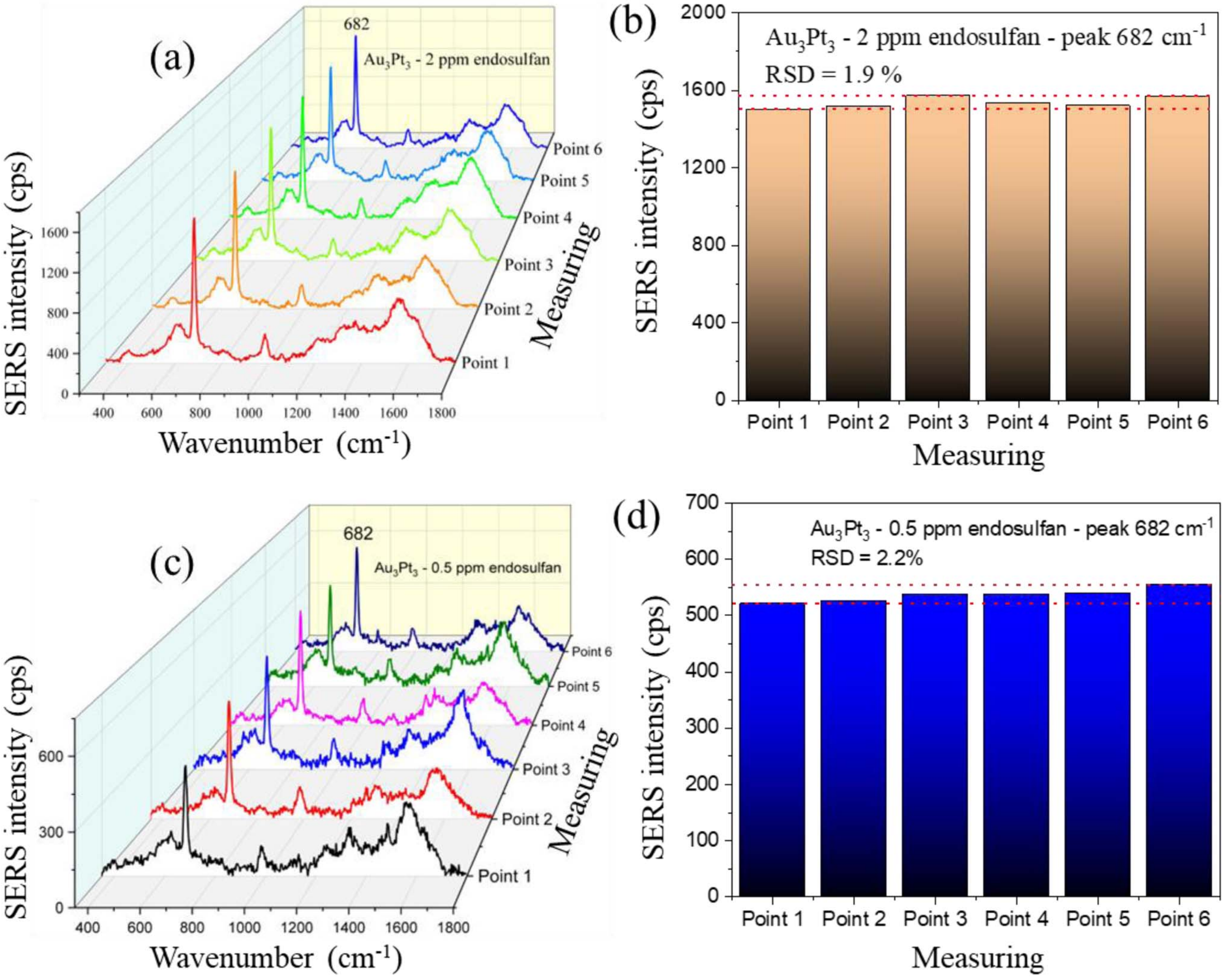

Fig. 10 SERS spectra of 2 ppm (a) and 0.05 ppm (b) ES from 6 different points on the Au_3Pt_3 substrate, (c) and (d) relative standard deviation (RSD) from 682 cm^{-1} peak resulting from Fig. 10a and b, respectively.

field enhancement and a relatively high average field enhancement, making them an excellent platform for SERS substrate.

Fig. 9c plots the SERS spectra for different ES concentrations, ranging from 0.05 ppm to 2 ppm of ES on the Au_3Pt_3 surface. It can be seen that the SERS intensity from Au_3Pt_3 increases with ES concentration. Fig. 9d shows a fairly linear relationship between logarithm of SERS intensity ($\log I$) and logarithm of ES concentration ($\log C$) as the following equation:

$$\log I = 2.911 + 0.534\log C \tag{6}$$

In the range of 0.05–2 ppm with the standard correlation coefficient $R^2 = 0.9981$. Although satisfactory linearity was obtained under controlled conditions, future quantitative optimization may incorporate ratiometric SERS or isotope-labeled internal standards to improve analytical robustness in complex sample matrices. This may be particularly useful for reducing signal variability and matrix-related interference in complex practical samples. In Table 2, a comparison with published reports showed that the detection performance of AuPt NPs with SERS technique is better than other SERS substrates in identifying ES. ES is a very challenging analyte, due to its poor affinity to metal surfaces, which is also the reason why scarce results can be found in the literature.

We further studied the limit of detection of the SERS substrate for ES. Notably, SERS signal can be observed for ES concentration as low as 0.05 ppm (Fig. 9e). The characteristic peak of ES at lowest concentration on the Au_3Pt_3 surface is still observable. Using a signal-to-noise ratio of 2 to 1, the limit of detection (LOD) for ES was determined as 0.05 ppm, lower than the allowable limit of residue in fruit by the European Union at 5×10^{-4} mg ml^{-1}.[51] This result indicates that the Au_3Pt_3-based SERS substrate has promising potential for sensitive ES detection at low concentration. However, further validation in real samples will be necessary before practical residue analysis in food and environmental matrices can be fully established.

The detection homogeneity of the SERS substrate for ES was tested by collecting the SERS spectra at 6 different spots on the same sample surface (Au_3Pt_3) as shown in Fig. 10(a and c). The highest-intensity characteristic peak of 682 cm^{-1} was chosen to

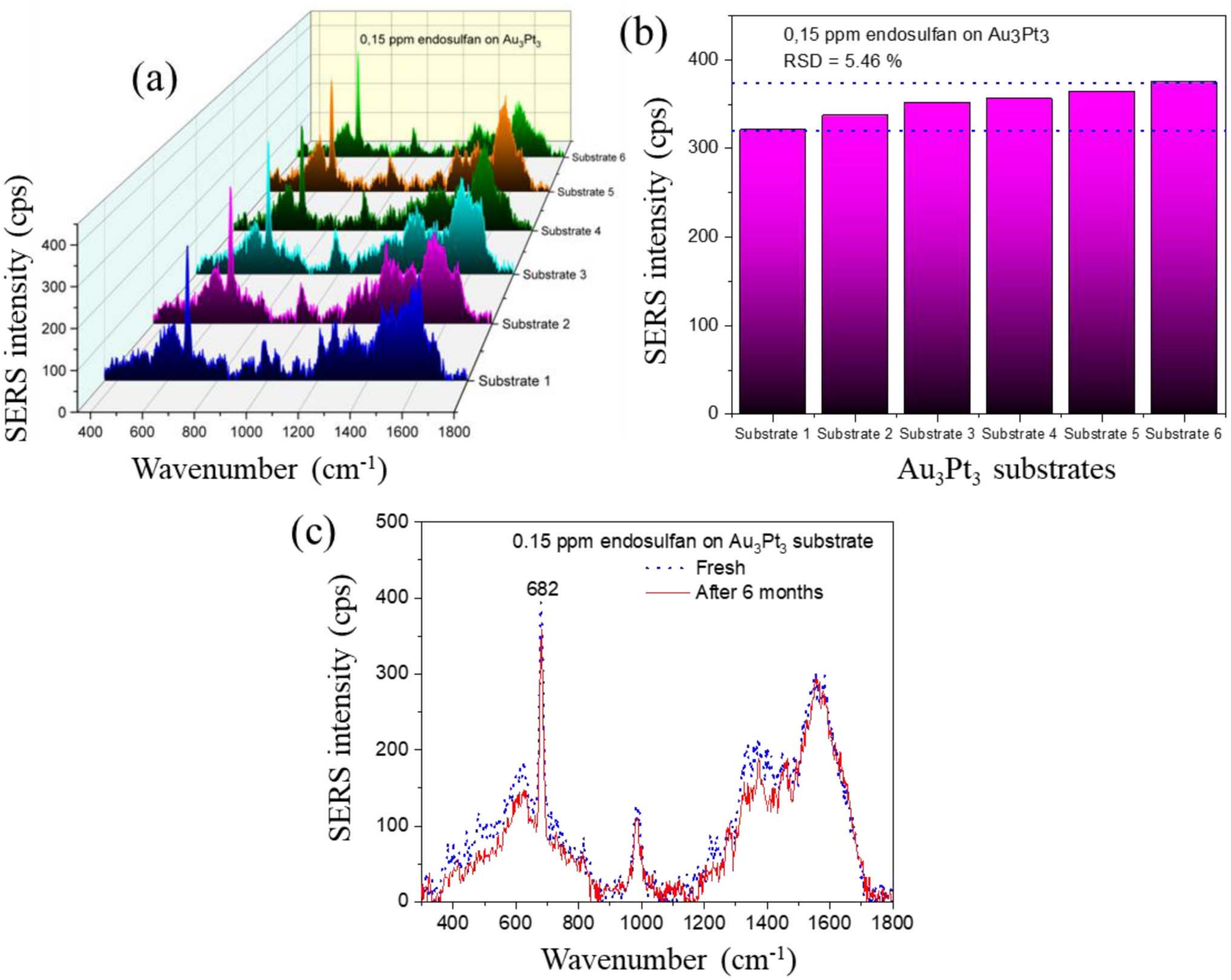

Fig. 11 (a) SERS spectra of endosulfan molecules at a concentration of 0.15 ppm from six independently prepared Au_3Pt_3 substrates, (b) histogram of the peak intensity at 682 cm^{-1} from (a), (c) stability of the Au_3Pt_3 substrate after 6 months of preservation.

calculate the relative standard deviation (RSD) and observe the uniformity field enhancement of the SERS substrate. The calculated RSD is as low as 1.9% for 2 ppm ES (Fig. 10b) and 2.2% for 0.05 ppm ES (Fig. 10d), so Au_3Pt_3 substrate showed good homogeneity for ES detection.

For practical application, reproducibility is one of the essential parameters for fabricated SERS substrates. Fig. 11a depicts the 3D SERS spectra of 0.15 ppm ES collected from 6 different Au_3Pt_3 substrates, and Fig. 11b shows their corresponding histogram.

The relative standard deviation (RSD) of SERS intensity for 682 cm^{-1} peak was 5.46%. This RSD indicates the small variation in SERS intensity from substrate to substrate. The Au_3Pt_3 substrates possess the high EF and good reproducibility, so to be excellent candidates for ES detection. Fig. 11c shows the SERS spectra after six months of aging, the Raman signal intensity decreased by 9.09% relative to that measured immediately after fabrication, demonstrating that the Au_3Pt_3 substrate possesses outstanding stability and is suitable for long-term storage under ambient conditions. This stability may be related to the structural robustness of the AuPt nanomaterial and the relatively stable sensing layer formed on the glass substrate. Notably, a level of durability that is rarely observed in conventional colloidal systems, which are prone to aggregation and instability. This good storage stability suggests that the Au_3Pt_3 substrate is a promising candidate for practical sensing applications in which reproducibility and shelf-life are important. Nevertheless, further validation under more diverse operating conditions will be required for broader real-world use.

The current stability assessment was performed under ambient storage conditions. Future work will examine the SERS response under high humidity, temperature fluctuation, and other challenging environmental conditions to further assess substrate robustness for broader practical use. Although this work focuses on endosulfan, the AuPt substrate may also be applicable to other Raman-active pesticides and related organic contaminants. Nevertheless, because metal-based SERS substrates are inherently cross-sensitive, selective identification in mixed-analyte systems will require additional strategies such as surface functionalization, competitive adsorption studies, and chemometric spectral discrimination.

From a practical perspective, although Au and Pt are relatively expensive noble metals, the present substrate is prepared by a simple solution-based route and requires only a small sensing-layer loading. In addition, its good reproducibility and storage stability may partially offset the higher intrinsic material cost relative to less stable conventional systems. For complex real samples, matrix interference must also be considered. In such cases, sample pretreatment and analyte separation prior to SERS measurement, for example by solvent extraction and, where appropriate, thin-layer chromatography (TLC), may help improve analytical selectivity and reliability.

3.5. Proposed SERS mechanism of AuPt bimetallic

The enhanced SERS activity of the AuPt substrate is most likely governed by a combination of electromagnetic and chemical effects, in which the electromagnetic mechanism (EM) is considered dominant under the present experimental conditions, while chemical contributions are regarded as supportive.[52–55] In general, the EM mechanism originates from the amplification of the local electric field near plasmonic nanostructures under light excitation, especially at interparticle junctions where localized hotspots are generated.[54,55] Since Au is a typical plasmonic metal with strong visible-light response, the Au-containing component in the AuPt system is expected to play a major role in the enhancement process.[56]

In the present work, the composition-dependent SERS results show that the Au_3Pt_3 sample exhibits the strongest Raman enhancement toward endosulfan. TEM/HRTEM observations indicate that the AuPt nanoparticles are distributed discontinuously with particle sizes of about 10–20 nm, forming numerous interparticle nanogaps. Such structural features are favorable for hotspot generation and near-field coupling, thereby enhancing the local electromagnetic field and increasing the Raman signal of adsorbed ES molecules.[32,42,55] Therefore, the superior SERS response of Au_3Pt_3 is likely associated not only with its Au : Pt compositional balance but also with its favorable nanoparticle morphology and gap structure.

Besides the dominant EM contribution, alloying Au with Pt may modify the interfacial physicochemical and electronic properties of the substrate. Bimetallic nanocrystals are known to combine the properties of two different metals and may exhibit synergistic effects that differ from those of their monometallic counterparts.[23,25,26,57] In AuPt systems, Au provides plasmonic response, whereas Pt contributes chemical stability and may influence surface-related electronic behavior.[27,56] Such alloying-induced effects can affect analyte adsorption and molecular polarizability, thereby contributing to the observed SERS enhancement.

The energy-level diagram in Fig. 12 provides additional support for this interpretation. Under 532 nm excitation, the photon energy is lower than the HOMO–LUMO gap of the ES molecule, indicating that direct molecular resonance is unlikely. Therefore, if a chemical contribution exists, it is more reasonably attributed to interfacial charge-transfer-related effects rather than to intrinsic resonance Raman

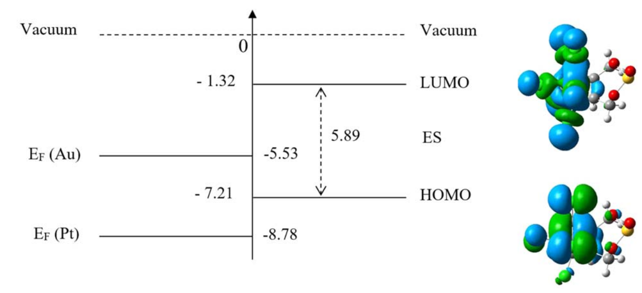

Fig. 12 Schematic energy-level alignment of endosulfan (ES) relative to the Fermi levels of Au and Pt, together with the calculated LUMO and HOMO isosurfaces of ES. The HOMO–LUMO gap of ES is larger than the photon energy of the 532 nm excitation laser, suggesting that direct molecular resonance is unlikely under the present experimental conditions.

enhancement of ES.[52,58–60] At the same time, Fig. 12 should be regarded as a schematic interpretation of the possible electronic interaction pathway rather than direct proof that CM is the dominant enhancement mechanism. Based on the present experimental evidence, Au–Pt electronic interaction and molecule-surface coupling may provide a supportive contribution, whereas the main enhancement is still assigned to the electromagnetic mechanism.

Overall, the current results support a synergistic EM-CM scenario in which the electromagnetic mechanism is dominant, while chemical effects associated with Au–Pt alloying and interfacial adsorption may play a secondary role. This interpretation is consistent with the plasmonic behavior of the Au-containing nanoparticles, the composition-dependent SERS response, the favorable morphology of the Au_3Pt_3 substrate, and the schematic energy-level relationship shown in Fig. 12.

4. Conclusions

In summary, bimetallic AuPt nanoparticles with sizes of approximately 10–20 nm were successfully synthesized from $HAuCl_4$ and H_2PtCl_6 *via* a facile reduction route and systematically characterized by TEM, HRTEM, EDS, XRD, UV-vis, and Raman spectroscopy. The obtained AuPt-based SERS substrate exhibited high sensitivity toward endosulfan detection over the concentration range of 0.05–2 ppm, with a detection limit of 0.05 ppm, good reproducibility, signal uniformity, and storage stability. Among the investigated compositions, the AuPt sample with an Au : Pt molar ratio of 1 : 1 showed the best SERS performance, giving an enhancement factor of about 14.3×10^6, which was higher than those of the corresponding monometallic Au and Pt substrates.

The enhanced performance is likely associated with the combined effects of alloy composition and favorable nanoparticle morphology, particularly the discontinuous particle distribution and the resulting interparticle nanogaps that promote hotspot generation. Based on the present results, the electromagnetic contribution is considered to be the dominant enhancement mechanism, while electronic interactions between Au, Pt, and the adsorbed molecules may also provide a supportive contribution. Although Au and Pt are relatively expensive noble metals, the present substrate offers several compensating advantages, including simple preparation, low sensing-layer consumption, good reproducibility, and improved stability. Overall, this work demonstrates that AuPt alloy nanoparticles are a promising SERS-active platform for sensitive endosulfan detection. Future studies should focus on quantitative robustness, complex-sample validation, mixed-analyte selectivity, and optimization of noble-metal loading and fabrication scalability.

Author contributions

Nguyen Dac Dien, Vuong Truong Xuan, Thi Thu Thuy Nguyen: writing original draft, formal analysis, validation and reviewing; Pham Thi Nga, Tran Thu Trang, Ngo Thi Lan, Nguyen Van Hao, Nguyen Thi Dung: data curation, investigation; Thi Thu Ha Pham, Xuan Hoa Vu: conceptualization, supervision, project administration, funding acquisition, review and editing, resources; Tran Thi Kim Chi, Tran Thi Huong Giang, Trinh Danh Hung: validation, software; Lai Tong Anh Kiet, Hoang Duy Long, Do Duc Nguyen, Pham The Tan, Nguyen Vu Anh Tuyet, Truong Duc Cuong: data curation, methodology.

Conflicts of interest

The authors declare that they have no known competing financial interests or personal relationships that could have appeared to influence the work reported in this paper.

Data availability

The datasets used and/or analyzed during the current study are available from the corresponding author upon reasonable request. In addition, all the data generated or analyzed during this study are included in this article.

Acknowledgements

This research was funded by the TNU-University of Sciences for the research group NNCM.ĐHKH.2025.02.

References

1 F. A. Gunther, *Residue Reviews – Volume 3: Residues of Pesticides and Other Foreign Chemicals in Foods and Feeds*, Springer-Verlag OHG, Berlin, 1963.
2 Y. Wang, Y. Guo, Y. Hu, Y. Sun and D. Xu, *Sci. Total Environ.*, 2020, **731**, 139234.
3 J. Abraham and S. Silambarasan, *Pestic. Biochem. Physiol.*, 2014, **116**, 24–31.
4 J. D. Santamaria-Juarez, M. Á. Hernández, G. I. Hernández, K. M. Álvarez, E. Rubio, R. Portillo, M. d. l. Á. Velasco, J. F. Aquino and V. Petranovskii, *Minerals*, 2024, **14**(7), 643.
5 K. Rawat, A. Srivastava, S. Tandon and G. P. Singh, *Anal. Sci.*, 2023, **39**(4), 431–439.
6 Z. Lin and L. He, *Curr. Opin. Food Sci.*, 2019, **28**, 82–87.
7 E. V. Solovyeva, *Nanobiotechnol. Rep.*, 2024, **19**(1), 1–16.
8 J. Zhu and J. Yin, *Carbon Lett.*, 2022, **32**, 629–637.
9 Y. Wan, Q. Liu, Z. Xu, J. Li, H. Wang, M. Xu, C. Yan, X. Song, X. Liu and H. Wang, *Carbon Lett.*, 2024, **34**(4), 1143–1154.
10 J. Langer, D. Jimenez de Aberasturi, J. Aizpurua, R. A. Alvarez-Puebla, B. Auguié, J. J. Baumberg, G. C. Bazan, S. E. J. Bell, A. Boisen and A. G. Brolo, *ACS Nano*, 2019, **14**(1), 28–117.
11 J. Yi, E.-M. You, R. Hu, D.-Y. Wu, G.-K. Liu, Z.-L. Yang, H. Zhang, Y. Gu, Y.-H. Wang and X. Wang, *Chem. Soc. Rev.*, 2025, **54**, 1453–1551.
12 Q. Zhang, D. A. Blom and H. Wang, *Chem. Mater.*, 2014, **26**(17), 5131–5142.
13 A. Karmakar, S. Mandal, W. Hossain, M. Ghosh, S. Chakraborty, T. Goswami, P. Ghosh and A. Mandal, *J. Mol. Struct.*, 2023, **1274**, 134383.

14 B. Liu, K. Li, Y. Luo, L. Gao and G. Duan, *Chem. Eng. J.*, 2021, **420**, 129881.

15 A. Zhu, Y. Xu, S. Ali, Q. Ouyang and Q. Chen, *LWT–Food Sci. Technol.*, 2021, **150**, 111978.

16 A. Falamas, I. A. Brezestean, N. Tosa, S. Boca and C. Farcau, *Nano Express*, 2024, **5**(4), 045006.

17 I. A. Brezestean, N. Tosa, A. Falamas, D. Cuibus, C. M. Muntean, A. Bende, B. Cozar, C. Berghian-Grosan and C. Farcău, *Front. Chem.*, 2022, **10**, 915337.

18 O. Douass, B. Samoudi, O. Bendaou and S. Sanchez Cortes, *Egypt. J. Chem.*, 2022, **65**(131), 133–150.

19 H. Chen and C. Hao, *Molecules*, 2025, **30**(4), 829.

20 X. Zhao, S. Wang, K. Yang, X. Yang and X. Liu, *J. Colloid Interface Sci.*, 2023, **633**, 11–23.

21 N. Kang, Q. Wang, R. Djeda, W. Wang, F. Fu, M. M. Moro, M. D. L. A. Ramirez, S. Moya, E. Coy, L. Salmon, J.-L. Pozzo and D. Astruc, *ACS Appl. Mater. Interfaces*, 2020, **12**(48), 53816–53826.

22 C. Xia, W. He, X. F. Yang, P. F. Gao, S. J. Zhen, Y. F. Li and C. Z. Huang, *Anal. Chem.*, 2022, **94**(39), 13440–13446.

23 J. Geng, J. Che, Y. Weng, J. Zhou, X. Yang and Q. Fan, *Alex. Eng. J.*, 2025, **118**, 306–314.

24 X. Wang, C. Chen, G. I. N. Waterhouse, X. Qiao, Y. Sun and Z. Xu, *Food Chem.*, 2024, **453**, 139665.

25 D. Huang, L. Li, S. Wei, K. Yin, W. Shang, X. Hou and L. Wu, *Microchem. J.*, 2025, **213**, 113608.

26 R. Zhang, S. Xie, J. Yang, L. Zhang, R. Xiong, H. Sun, H. Zhang, M. Jiang and Y. He, *Microchem. J.*, 2024, **207**, 111990.

27 H. Ze, X. Chen, X.-T. Wang, Y.-H. Wang, Q.-Q. Chen, J.-S. Lin, Y.-J. Zhang, X.-G. Zhang, Z.-Q. Tian and J.-F. Li, *J. Am. Chem. Soc.*, 2021, **143**(3), 1318–1322.

28 J. Cui, P. Zhang, Y. Zhao, M. Gu, J. Tan, H. Zhang and B. Wang, *J. Environ. Chem. Eng.*, 2026, **14**, 122278.

29 X. Zhao, S. Han, C. Chen, X. Lv, J. Li and C. Chen, *Spectrochim. Acta, Part A Mol. Biomol. Spectrosc.*, 2025, **348**, 127165.

30 T. Wu, L. Lv, N. Zhang, J. Fu, Y. Du, X. Ren and Q. Wei, *Sens. Actuators, B Chem.*, 2025, **447**, 138805.

31 T. A. Quang, T. M. C. Tran, T. M. Aminabhavi, L. Gnanasekaran, Y. Vasseghian and S.-W. Joo, *J. Environ. Manag.*, 2025, **373**, 123561.

32 W. Lu, Y. Jiang, X. Yao, Y. Yu, W. Shen, M. Yang, X. Huang and X. Tang, *RSC Adv.*, 2025, **15**(9), 6663–6667.

33 T. T. H. Pham, N. D. Dien and X. H. Vu, *RSC Adv.*, 2021, **11**(35), 21475–21488.

34 T. T. H. Pham, X. H. Vu, N. D. Dien, T. T. Trang, N. Van Truong, T. D. Thanh, P. M. Tan and N. X. Ca, *RSC Adv.*, 2020, **10**(41), 24577–24594.

35 X. H. Vu, N. D. Dien, T. T. H. Pham, N. Van Truong, N. X. Ca and V. Van Thu, *RSC Adv.*, 2021, **11**(24), 14596–14606.

36 S. Pang, T. Yang and L. He, *Trends Anal. Chem.*, 2016, **85**, 73–82.

37 J. Sitjar, J.-D. Liao, H. Lee, B. H. Liu and W.-E. Fu, *Nanomaterials*, 2019, **9**(5), 664.

38 C. Fasolato, *Surface Enhanced Raman Spectroscopy for Biophysical Applications Using Plasmonic Nanoparticle Assemblies*, Springer, Switzerland, 2018.

39 S. Talu, D. N. Trong and L. V. Truong, *J. Nanomater. Appl.*, 2025, **1**(1), 1–16.

40 X. Fu, Z. Li, J. Zhao, J. Yang, G. Zhu, G. Li and P. Huo, *J. Colloid Interface Sci.*, 2024, **676**, 127–138.

41 E. R. Mawarnis, S. M. El-Bahy, A. Y. A. Al-She'irey, L. Roza, I. H. El Azab, G. A. M. Mersal, Z. M. El-Bahy, M. M. Ibrahim and A. A. Umar, *Inorg. Chem. Commun.*, 2022, **143**, 109737.

42 M. Herran, A. Sousa-Castillo, C. Fan, S. Lee, W. Xie, M. Döblinger, B. Auguié and E. Cortés, *Adv. Funct. Mater.*, 2022, **32**(38), 2203418.

43 C. Yang, D. Zhang, W. Zhao, M. Cui, R. Liang, Q. Ou and S. Zhang, *J. Alloys Compd.*, 2020, **835**, 155334.

44 T.-Y. Yang, G.-X. Yu, J. Liu, X. Li, L. Chen and Z. Guo, *Sens. Actuators, B*, 2025, **426**, 137125.

45 Y. Liu, L.-Y. Zhu, P. Feng, C. Dang, M. Li, H.-L. Lu and L. Gao, *Sens. Actuators, B Chem.*, 2022, **367**, 132024.

46 N. A. Shad, H. Khadim, M. A. Tahir, M. F. Khan, S. Nazir, A. Rakha and A. Munawar, *Mater. Chem. Phys.*, 2025, **338**, 130654.

47 E. L. Ru and P. Etchegoin, *Principles of Surface Enhanced Raman Spectroscopy and Related Plasmonic Effects*, Elsevier, 2009.

48 J. Ding, Y. Yang, D. Kang, M. Zhang, J. Li, L. Kong and P. Song, *Spectrochim. Acta, Part A Mol. Biomol. Spectrosc.*, 2024, **310**, 123911.

49 E. C. Le Ru and B. Auguié, *ACS Nano*, 2024, **18**(14), 9773–9783.

50 M. K. Katlego, Electrochemical properties of carbon nanotubes/PANI/metal oxide nanoparticle nanocomposites towards electrocatalysis of some organochlorine pesticides, *Master of Science in Chemistry*, North-West University, South Africa, 2018.

51 F. Pan, H. Wu, J. Tang, L. Xiang and J. Wei, *Chem. Pap.*, 2022, **76**(9), 5571–5578.

52 N. Abu Bakar, M. Fronzi and J. G. Shapter, *Sensors*, 2024, **24**(2), 373.

53 S. Cong, X. Liu, Y. Jiang, W. Zhang and Z. Zhao, *Innov.*, 2020, **1**(3), 100051.

54 P. Prosposito, L. Burratti and I. Venditti, *Chemosens*, 2020, **8**(2), 26.

55 D. Cialla-May, A. Bonifacio, A. Markin, N. Markina, S. Fornasaro, A. Dwivedi, T. Dib, E. Farnesi, C. Liu and A. Ghosh, *Trends Anal. Chem.*, 2024, **181**, 117990.

56 K. Sytwu, M. Vadai and J. A. Dionne, *Adv. Phys.:X*, 2019, **4**(1), 1619480.

57 A. K. Yagati, A. Go, S. G. Chavan, C. Baek, M.-H. Lee and J. Min, *Bioelectrochemistry*, 2019, **128**, 165–174.

58 H. Park, S. Chun, J. H. Lee, J. Son, S. Kim, J. Choi, H. Ihee, H. Lee and J. Y. Park, *J. Am. Chem. Soc.*, 2025, **147**(39), 35913–35923.

59 M. Chen, Z. Ye, L. Wei, J. Yuan and L. Xiao, *J. Am. Chem. Soc.*, 2022, **144**(28), 12842–12849.

60 R. Aroca, *Surface-enhanced Vibrational Spectroscopy*, John Wiley & Sons, Ltd, England, 2006.